

# A SEMI-ANALYTICAL LINE TRANSFER (SALT) MODEL TO INTERPRET THE SPECTRA OF GALAXY OUTFLOWS

C. SCARLATA<sup>1</sup> AND N. PANAGIA<sup>2,3,4</sup>

*Draft version June 24, 2021*

## ABSTRACT

We present a Semi-Analytical Line Transfer model, SALT, to study the absorption and re-emission line profiles from expanding galactic envelopes. The envelopes are described as a superposition of shells with density and velocity varying with the distance from the center. We adopt the Sobolev approximation to describe the interaction between the photons escaping from each shell and the remaining of the envelope. We include the effect of multiple scatterings within each shell, properly accounting for the atomic structure of the scattering ions. We also account for the effect of a finite circular aperture on actual observations. For equal geometries and density distributions, our models reproduce the main features of the profiles generated with more complicated transfer codes. Also, our SALT line profiles nicely reproduce the typical asymmetric resonant absorption line profiles observed in starforming/starburst galaxies whereas these absorption profiles cannot be reproduced with thin shells moving at a fixed outflow velocity. We show that scattered resonant emission fills in the resonant absorption profiles, with a strength that is different for each transition. Observationally, the effect of resonant filling depends on both the outflow geometry and the size of the outflow relative to the spectroscopic aperture. Neglecting these effects will lead to incorrect values of gas covering fraction and column density. When a fluorescent channel is available, the resonant profiles alone cannot be used to infer the presence of scattered re-emission. Conversely, the presence of emission lines of fluorescent transitions reveals that emission filling cannot be neglected.

*Subject headings:* galaxies: ISM — ISM: structure

## 1. INTRODUCTION

The mechanical and radiative energy (from massive star winds and supernova explosions) injected in the interstellar medium (ISM) of galaxies is expected to drive gas outflows around regions of active star-formation. These outflows are indeed observed both on the scale of individual H II regions as well as on full-galaxy scales. Outflows are currently invoked as the principal mechanism regulating the galactic baryonic cycle (i.e., the balance between the gas accretion rate and the star-formation rate) in state-of-the-art galaxy formation models (e.g. Oppenheimer et al. 2010; Davé et al. 2011; Lilly et al. 2013). Whether or not the observed outflows are actually able to do the job is, however, still unclear. In fact, although outflow-regulated models are able to broadly reproduce some of the fundamental correlations observed in massive galaxies, recent studies have pointed out the existence of a fundamental problem with the evolution of low mass ( $M_* < 10^{9.5} M_\odot$ ) galaxies (Weinmann et al. 2012). This difficulty appears to indicate that crucial feedback processes are modeled incorrectly, since it is precisely in this low-mass regime that feedback-induced outflows are expected to have the strongest impact.

What is lacking at this point are robust observational

constraints on the physical properties of galaxy outflows and how these depend on the galaxy star-formation rates, stellar masses, and so on. In order to characterize how effective feedback is in quenching the star-formation (by, e.g., heating the gas and/or completely remove it from a galaxy dark matter halo) we need to be able to probe the kinematics of the outflows, their density structure, and their extent. Absorption line studies against the strong UV continuum produced in the star-forming regions can probe the neutral and ionized components of the outflows, with numerous resonant transitions in low and high ionization metals (such as, Si II, C II, Mg II, C III, Fe II, and C IV; e.g., Rupke et al. 2005; Martin 2005; Sato et al. 2009; Weiner et al. 2009; Rubin et al. 2010; Steidel et al. 1996; Shapley et al. 2003).

Recent studies show that outflowing gas moving with velocities up to several hundreds of  $\text{km s}^{-1}$  is common in star-forming galaxies (e.g., Pettini et al. 2002; Martin 2005). Generally, these studies use standard absorption-line analysis (e.g. Savage & Sembach 1991), where the velocity of the outflowing material is determined by the amount of blueshift observed in the resonant absorption lines (typically UV lines, but absorption of Na-D lines has been used). Recent observations, however, have revealed the presence of numerous resonant and fluorescent emission lines associated with the blueshifted resonant absorptions (e.g., Weiner et al. 2009; France et al. 2010; Rubin et al. 2011; Jones et al. 2012; Erb et al. 2012; Martin et al. 2012, 2013; Kornei et al. 2013). Although originally interpreted as the result of photoionization by weak AGNs (e.g., Weiner et al. 2009), these lines are now believed to be the result of scattered resonant photons in an expanding envelope around galaxies (Rubin et al.

<sup>1</sup> Minnesota Institute for Astrophysics, School of Physics and Astronomy, University of Minnesota, 316 Church str SE, Minneapolis, MN 55455, USA

<sup>2</sup> Space Telescope Science Institute, 3700 San Martin Drive, Baltimore, MD 21218, USA, panagia@stsci.edu

<sup>3</sup> INAF-NA, Osservatorio Astronomico di Capodimonte, Salita Moiariello 16, 80131 Naples, Italy

<sup>4</sup> Supernova Ltd, OYV #131, Northsound Rd., Virgin Gorda VG1150, Virgin Islands, UK

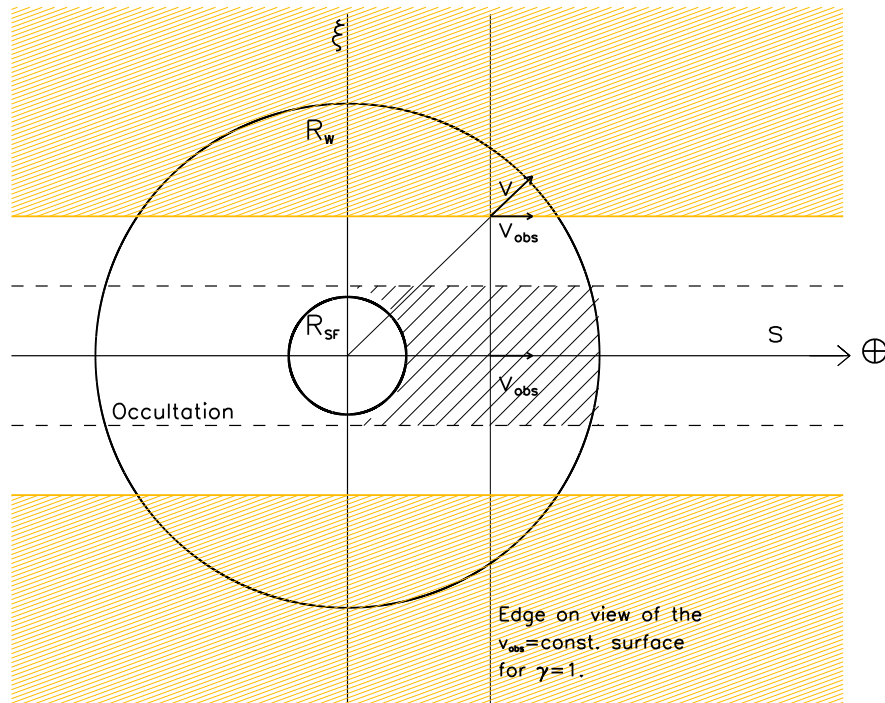


FIG. 1.— Side view of the outflow model. We consider a spherical galaxy (with radius  $R_{SF}$ ) surrounded by an expanding envelope with a velocity increasing radially with the distance from the center. For  $r > R_W$  the gas velocity is  $v_\infty$ . The shaded yellow area shows the size of the aperture of radius  $R_{apert}$ . The dotted vertical line indicates the edge-on view of the plane with constant observed velocity ( $v_{obs}$ ).

2011; Erb et al. 2012; Martin et al. 2013).

The scattered re-emission into the line of sight affects the velocity measurements based on pure absorption lines analysis, as well as mimic a partial covering fraction of the outflowing gas (e.g., Prochaska et al. 2011). In these cases, it is crucial to be able to consistently model both the resonant absorption as well as the associated resonant and (if present) fluorescent emission originating from the same ionic species. Steps in this direction have been taken by Rubin et al. (2011), who pioneered the study of outflows in emission using resonantly-scattered MgII, and Fe lines. Prochaska et al. (2011) used Monte Carlo radiative transfer techniques to study the nature of resonant absorption and emission for winds, accounting for the effects of resonant scattering and fluorescence.

In this paper we go a step forward and develop a Semi-Analytical Line Transfer (hereafter referred to as SALT) model to interpret the absorption/scattered emission line profiles resulting from extended galactic outflows. We assume that the Sobolev approximation holds, and we account for multiple scattering within the outflow with a simple statistical approach. As an example of an application of the model, we apply SALT to multiple transitions in the  $\text{Si}^+$  ion observed in the stack spectrum of

$z \sim 0.3$  Ly $\alpha$  emitters. We show how our model is able to consistently reproduce the profiles of both the absorption and resonant and fluorescent emission lines and thus constrain the outflow velocity- and density-fields. Although rather simplified, the SALT model can be used to gain a more physical understanding of the outflowing gas, in both local and high redshift galaxies. We focus here on a few specific lines of  $\text{Si}^+$  ion, however, the models are readily applicable to any other ions.

The paper is organized as follows. In Section 2 we present the derivation of the semi analytical line profile for an outflowing spherical shell. The model is compared with the observed stacked spectrum in Section 3, and the results are discussed in Section 4. We offer our conclusions in Section 5.

## 2. P-CYGNI PROFILE FROM A SPHERICAL EXPANDING ENVELOPE

In spherical outflows, such as those produced in winds from early type stars, resonant lines are characterized by the well understood P-Cygni profile (e.g., Castor 1970; Castor & Lamers 1979). The profile shows both an emission and an absorption component. The absorption is created in the material between the source and

the observer, while the emission is produced by scattering photons into the line of sight. For spherical outflows, the velocity profile of the absorption component will be blueshifted relative to the systemic velocity of the source and will depend on the density and velocity fields of the absorbing material. Because of the spherically symmetric geometry, the emission component will be centered at the systemic velocity of the source and thus will contribute to fill in the absorption at negative velocities. This effect, well known in the context of stellar winds, has generally been neglected in the context of absorption line studies of galaxies. Recently, however, a few studies have emphasized the importance of properly accounting for scattered re-emission in studies of galaxy absorption line spectra. These studies have also highlighted how the emission line features can be used as powerful diagnostics of the geometry and physical conditions of galaxy outflows both in the local and high-redshift Universe (Rubin et al. 2011; Prochaska et al. 2011; Erb et al. 2012; Martin et al. 2013). The goal of this paper is to present a semi-analytical line transfer (SALT) model that can be used to consistently interpret the absorption and emission line profiles of both resonant and fluorescent transmissions observed in galactic spectra. The line profiles are modeled for outflow geometries similar to those introduced by the recent works of Rubin et al. (2011); Prochaska et al. (2011); Erb et al. (2012); Martin et al. (2013).

In this Section we first describe the basic assumptions to derive the line profiles in single scattering approximation Scuderi et al. (following 1992). We then modify the wind model to include a more realistic description of the scattering process by relaxing the single scattering approximation. We also include the possibility of re-emission in the fluorescent channel, different envelope geometries and effect of a finite aperture.

### 2.1. The basic model

To build our SALT model we start with the simplest description for the gas/star configuration. We approximate a galaxy as a spherical source of UV radiation with radius  $R_{SF}$  (i.e., where the bulk of star-formation occurs), surrounded by an expanding envelope of gas, extending to  $R_W$ . In the following we will refer to the expanding envelope as the “galactic wind”. Prochaska et al. (2011) use a Monte Carlo radiative transfer technique to derive the absorption line profiles resulting from similar galactic winds. In what follows, we simplify their calculations by computing semi-analytical expressions for the line profiles (including the effects of fluorescent emission and spectroscopic aperture size). Martin et al. (2013) use a similar outflow model to study the extended scattered emission from galactic outflows at  $z \sim 1$ , considering the effects of a clumpy expanding medium on the derived mass outflow rate. Here, we build upon these works, and we develop a semi-analytical algorithm to simply but accurately calculate the expected line profiles originating in extended outflows. Our results can be used to easily model galactic extended outflows commonly observed in local and high redshift galaxies.

In Figure 1 we show the geometry of the wind and the definition of the coordinate system. The coordinates  $\xi$  and  $s$  are given in units of  $R_{SF}$ , so that in Figure 1 the dashed line tangential to the galaxy has  $\xi = 1$ . We also

introduce the normalized radial coordinate  $\varrho = r/R_{SF}$  ( $\varrho = \sqrt{\xi^2 + s^2}/R_{SF}$ ). A given point P in the envelope is identified by the pair of coordinates  $\varrho, \theta$ , where  $\theta$  is the angle between the direction of  $r$  and the line of sight to the observer.

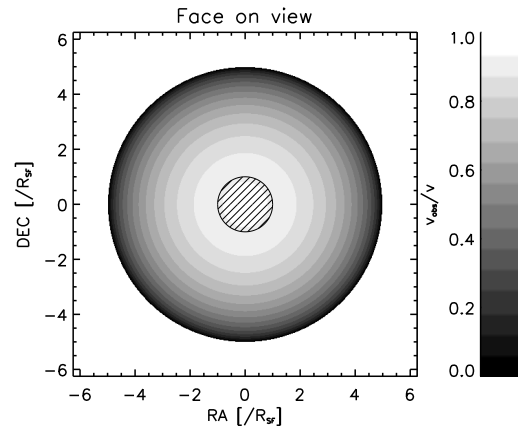


FIG. 2.— Iso-velocity contours of observed velocity for a shell moving at radial velocity  $v$ . The observed velocity ranges from  $v_{\text{obs}} = v$  at the center of the shell, to  $v_{\text{obs}} = 0$  at the edge.

We consider a velocity field where the velocity ( $v$ ) increases with  $r$  as a power law of exponent  $\gamma$ :

$$v = v_0 \left( \frac{r}{R_{SF}} \right)^\gamma \text{ for } r \leq R_W = R_{SF} \left( \frac{v_\infty}{v_0} \right)^{1/\gamma}; \quad (1)$$

$$v = v_\infty \text{ for } r \geq R_W; \quad (2)$$

where  $v_0$  is the wind velocity at the surface of the star-forming region (i.e., at  $R_{SF}$ ), and  $v_\infty$  is the terminal velocity of the wind at  $R_W$ .

When the velocity gradient in the expanding envelope is large, photons will interact with the outflowing material only where the absorbing ions are exactly “at resonance” due to their Doppler shift (this is a condition also known as “Sobolev’ approximation”, e.g., Grinin 2001). In this case, the radiative transport of the line photons

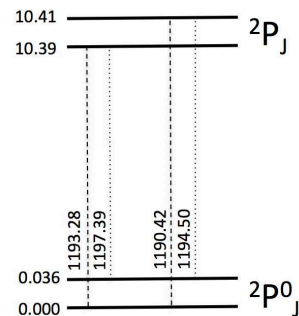


FIG. 3.— Energy levels of  $\text{Si}^+$ .

can be reduced to a local problem, and the optical depth for absorption ( $\tau$ ) can be evaluated at the *interaction surface*, which is defined in terms of the velocity as:

$$v = -c \frac{\Delta \nu}{\nu_0}; \quad (3)$$

where  $\nu_0$  is the resonance frequency of the line. The numerical results of Prochaska et al (2011) show that for the physical conditions of typical galaxy outflows, the Sobolev approximation is a justified assumption.

The wind optical depth at the interaction surface, can be written as a function of wavelength, wind parameters, and atomic constants, as follows (e.g., Castor 1970):

$$\tau(r) = \frac{\pi e^2}{mc} f_{lu} \lambda_{lu} n_l(r) \left[ 1 - \frac{n_u g_l}{n_l g_u} \right] \frac{r/v}{1 + \sigma \mu^2}; \quad (4)$$

where  $f_{ul}$  and  $\lambda_{lu}$  are the oscillator strength and wavelength, respectively, for the  $ul$  transition,  $\mu = \cos(\theta)$ , and  $\sigma = \frac{d \ln(v)}{d \ln(r)} - 1$  (see Table 1 for Si<sup>+</sup> atomic data). The expression for the optical depth can be simplified by assuming that 1) it does not depend on the angle  $\theta$  between a radius and the line of sight, 2) the above velocity law holds, 3) stimulated emission is negligible (i.e.,  $\left[ 1 - \frac{n_u g_l}{n_l g_u} \right] = 1$ ), and 4) the mass outflow rate is constant, so that  $n_l(r) \propto (vr^2)^{-1}$ . For  $\gamma = 1$ , and with these assumptions, we can write:

$$\tau(r) = \frac{\pi e^2}{mc} f_{lu} \lambda_{lu} n_0 \left( \frac{R_{SF}}{r} \right)^3 \frac{r}{v} \quad (5)$$

$$= \tau_0 \left( \frac{R_{SF}}{r} \right)^3 \quad (6)$$

and

$$\tau_0 = \frac{\pi e^2}{mc} f_{lu} \lambda_{lu} n_0 \frac{R_{SF}}{v_0}; \quad (7)$$

where  $n_0$  is the gas density at  $R_{SF}$  (for  $\gamma = 1$ ,  $n_l(r) = n_0 \left( \frac{r}{R_{SF}} \right)^{-3}$ ).

Now consider a thin shell located at a distance  $r = R_{SF} \left( \frac{v}{v_0} \right)^{1/\gamma}$ , moving with an intrinsic radial velocity  $v$ . The velocity measured by the observer, i.e. the component of the radial velocity along the line of sight to the observer ( $v_{\text{obs}} = v \cos \theta$ ) will depend on the position on the shell and in particular on the projected distance to the center. This is shown in Figure 2, where we plot contours of constant *observed* (i.e., projected) velocity from a shell moving outward with radial velocity  $v$ . For the sake of clarity, we show only the half of the shell moving toward the observer. The observed velocities range from  $-v$  at the projected center of the envelope (where the gas is moving directly toward us) to 0 at the projected distance  $r = r_v$  (where the shell is moving on the plane of the sky). Obviously, only the portion of the shell *in front* of the continuum disk (hatched area in Figures 2) will produce a net absorption in the spectrum (blueward of the line center) by scattering photons out of the line of sight.

Globally the shell will absorb a fraction  $E(v) = [1 - \exp(-\tau(v))]$  of the energy that, in terms of observed velocities ( $v_{\text{obs}} = v \cos \theta$ ), will be redistributed evenly over the velocity interval ( $v_{\text{min}}, v$ ). Here  $v_{\text{min}}$  is the projection of the shell velocity along the line of sight tangential to the galaxy (i.e., at  $\xi = 1$ ). Following Scuderi *et al.* (1992), we can compute  $v_{\text{min}}$  as:

$$v_{\text{min}} = v \cos \theta = v \frac{s(\varrho(v))}{\varrho(v)}. \quad (8)$$

Or, setting  $y = v/v_0$ , as:

$$y_{\text{min}} = y^{(\gamma-1)/\gamma} (y^{2/\gamma} - 1)^{1/2}. \quad (9)$$

Only shells with intrinsic radial velocities in the range from  $v_{\text{obs}}$  and  $v_1 = v_{\text{obs}}/\cos \theta$  (for  $\xi = 1$ ) can contribute to the absorption at  $v_{\text{obs}}$ . Setting  $x = v_{\text{obs}}/v_0$ ,  $y_1 = v_1/v_0$  can be computed by solving the equation:

$$y_1^2 (1 - y_1^{-2/\gamma}) = x^2. \quad (10)$$

Thus, we can write the absorption component of the profile, in units of the stellar continuum as:

$$I_{\text{abs,blue}}(x) = \int_{\max(x,1)}^{y_1} \frac{1 - e^{-\tau(y)}}{y - y_{\text{min}}} dy. \quad (11)$$

Surfaces of constant *observed* velocity can be described by the equation:

$$v_{\text{obs}} = v_0 \left( \frac{r}{R_{SF}} \right)^\gamma \cos \theta. \quad (12)$$

For the particular case of  $\gamma = 1$ , this equation describes parallel planes at distance  $r = R_{SF} \frac{v_{\text{obs}}}{v_0} \cos \theta$  from the center of the emitting region (see Figure 1).

### 2.1.1. Single scattering approximation

Resonant photons absorbed in the envelope can be detected when re-emitted toward the observer. Assuming that a re-emitted photon escapes a given shell without further interactions, we can compute the emission component of the line profile as follows. If the photons are re-emitted isotropically, then they will uniformly cover the range of projected velocities between  $\pm v$ . To describe the profile of this emission component, we divide the range of observed velocities into blueward and redward of the systemic velocity. The blue side of the emission profile originates in the half of the envelope approaching the observer (i.e.,  $s \geq 0$ ). For a given observed velocity, the emission will come from all shells with  $v > v_{\text{obs}}$ , and we can write:

$$I_{\text{em,blue}}(x) = \int_{\max(x,1)}^{y_\infty} \frac{1 - e^{-\tau(y)}}{2y} dy. \quad (13)$$

The red side of the profile is produced in the unocculted, receding portion of the envelope. Because of the occultation, however, only shells with velocities larger than  $v_{\text{min}}$  (see Eq. 9) will contribute to a given observed receding velocity:

$$I_{\text{em,red}}(x) = \int_{y_1}^{y_\infty} \frac{1 - e^{-\tau(y)}}{2y} dy. \quad (14)$$

Finally, the resulting P-Cyg profile for the ideal spherical outflows can be computed as:

$$I(x) = 1 - I_{\text{abs,blue}} + I_{\text{em,blue}} + I_{\text{em,red}}. \quad (15)$$

### 2.1.2. Fluorescent emission in single scattering approximation

Depending on the energy levels of the particular ionic species, the absorption of a resonant photon can result in the production of a fluorescent photon. This occurs when the electron decays into an excited ground level<sup>5</sup>. As an example, figure 3 shows the energy level diagram of the  $\lambda$  1190.42 and 1193.28Å Si<sup>+</sup> doublet. Resonant and fluorescent transitions are marked with dashed and dotted lines, respectively. We account for the fluorescent channel in the modeling of the line profile as follows.

For a bound electron, the probability of decaying into the lower level  $l$  is proportional to  $p_{ul} = A_{ul}/\sum_i A_{ui}$ , where  $A_{ui}$  is the spontaneous decay probability from the upper level  $u$  to the lower level  $i$ . Relevant  $A_{ui}$  values are given in Table 1. In the single scattering approximation, the resulting line profile accounting for the emission in the fluorescent channel becomes:

$$I(x) = 1 - I_{\text{abs,blue}} + p_R (I_{\text{em,blue}} + I_{\text{em,red}}) + p_F (I_{\text{em,blue}} + I_{\text{em,red}}), \quad (16)$$

where  $p_R$  and  $p_F$  are the probabilities that a photon is re-emitted in the resonant and the fluorescent channels, respectively. When only one fluorescent channel is available, as in the cases considered here,  $p_R + p_F = 1$ . The left panel in Figure 4 shows how the line profiles of the Si II doublet generated in an outflowing envelope change when the fluorescent channels are taken into account. When a fraction of the photons are re-emitted in the fluorescent transition, the filling effect of the resonant absorption due to photons scattered in the wind is substantially reduced for the 1190Å transition. It is only minimally reduced for the transition at 1193Å due to contamination from the fluorescent re-emitted photons at 1194.5Å (see Table 1). Because of the re-emission in the fluorescent channel, the total equivalent width of the resonant P-Cygni profile (i.e., including both the absorption and emission components) is negative (net absorption).

### 2.1.3. Accounting for multiple scatterings

More realistically, a photon re-emitted with the resonant energy will likely interact with the ions in the shell where it was created, resulting in multiple scattering events of a single photon within a given shell. Multiple scatterings will not change the shape of the absorption profile ( $I_{\text{abs,blue}}$ ), but will reduce the contribution of the re-emission in the resonant line, while enhancing the re-emission in the fluorescent channel (when this is available). The number of scatterings will clearly be a function of the ion density at any given point in the outflow. Thus, for our assumed density profile, this process will be more important in the internal regions of the

<sup>5</sup> In what follows, fluorescent transitions will be indicated with an \*.

outflow, where the density is highest. We account for multiple scatterings within a single shell, as follows.

We define the photon's escape probability from a shell of optical depth  $\tau(v)$  as (e.g., Mathis 1972):

$$\beta = (1 - e^{-\tau})/\tau, \quad (17)$$

Thus, for a shell with velocity  $v$ , a photon has a probability  $\beta$  of escaping the shell, and therefore –because of the underlying Sobolev approximation– escaping the outflow. Of all photons absorbed at resonance by the moving shell, a fraction  $p_F$  will be re-emitted in the fluorescent channel and escape. Of the fraction  $p_R$  of the photons re-emitted at resonance, a fraction  $1 - \beta$  will be absorbed again before they are able to escape the shell. Of these  $[p_R(1 - \beta)]$ , a fraction  $p_F$  will be converted into fluorescent photons and escape [i.e.,  $p_F p_R(1 - \beta)$ ]. Again, out of the resonantly re-emitted photons, a fraction  $1 - \beta$  will be re-absorbed within the shell, contribute to the fluorescent re-emission and escape the outflow. It can be easily shown that, for each shell, the fraction of absorbed photons converted into fluorescent photons is given by:

$$F_F(\tau) = p_F \sum_{n=0}^{\infty} [p_R(1 - \beta)]^n, \quad (18)$$

while the fraction of absorbed photons that are able to escape will be:

$$F_R(\tau) = p_R \beta \sum_{n=0}^{\infty} [p_R(1 - \beta)]^n. \quad (19)$$

Because  $p_R(1 - \beta) < 1$ , the summation of the geometric series in Equations 18 and 19 converges, and

$$F_F = p_F/[1 - p_R(1 - \beta)] \quad (20a)$$

$$F_R = \beta p_R/[1 - p_R(1 - \beta)]. \quad (20b)$$

Figure 5 shows the fraction of absorbed photons that escape in the fluorescent channel as a function of the shell optical depth for three representative values of  $p_F$ . Analogously to Eqns 13 and 14, the blue and red resonant-emission components become:

$$I_{\text{em,blue,MS}}(x) = \int_{\text{max}(x,1)}^{y_{\infty}} F_R(y) \frac{1 - e^{-\tau(y)}}{2y} dy \quad (21a)$$

$$I_{\text{em,red,MS}}(x) = \int_{y_1}^{y_{\infty}} F_R(y) \frac{1 - e^{-\tau(y)}}{2y} dy, \quad (21b)$$

while the blue and red fluorescent components can be written as:

$$I_{\text{em,blue,MS,F}}(x) = \int_{\text{max}(x,1)}^{y_{\infty}} F_F(y) \frac{1 - e^{-\tau(y)}}{2y} dy \quad (22a)$$

$$I_{\text{em,red,MS,F}}(x) = \int_{y_1}^{y_{\infty}} F_F(y) \frac{1 - e^{-\tau(y)}}{2y} dy. \quad (22b)$$

In the right panel of Figure 4 we show the effect of accounting for multiple scatterings on the line profiles of the

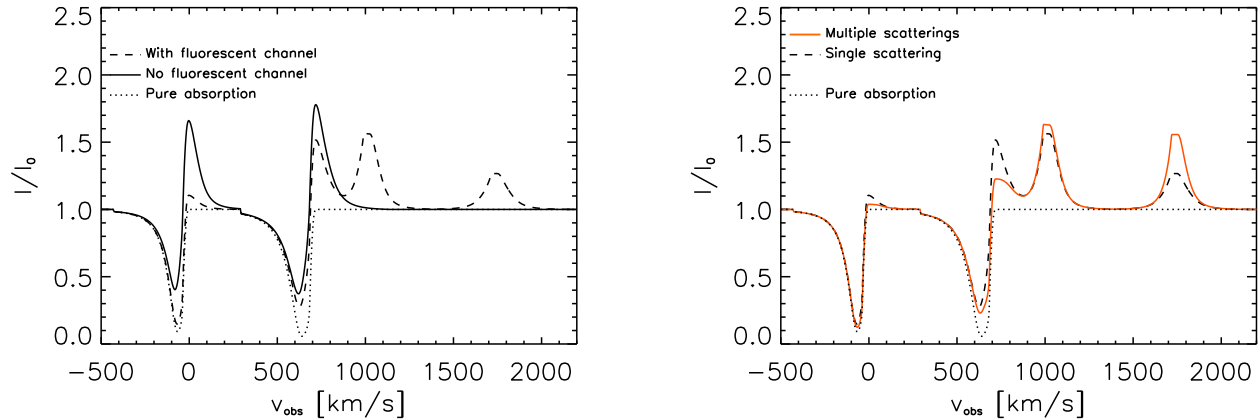


FIG. 4.— Left: Effect of fluorescent channel on the resonant P-Cygni profile. The Si<sup>+</sup> doublet line profiles are shown with and without the inclusion of the fluorescent emission (dashed and solid line respectively) for the single-scattering approximation. The pure absorption component of the profile is also shown for reference (dotted line). Right: Si<sup>+</sup> doublet profiles computed with single scattering approximation (black) and multiple scatterings (red).

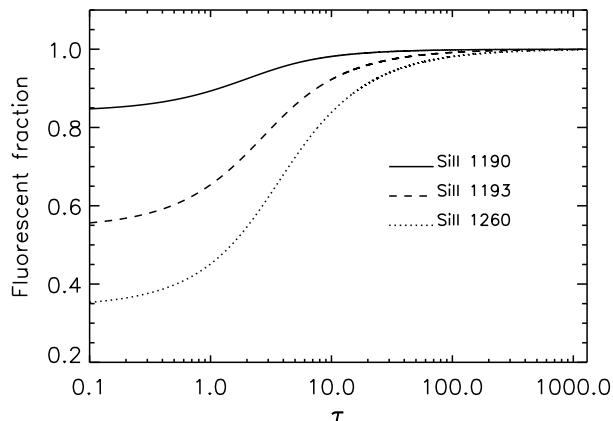


FIG. 5.— The fraction of absorbed resonant photons re-emitted in the fluorescent channel after multiple scatterings depends on the gas column density as well as on the transition probability. We show the calculations for three transitions of Si<sup>+</sup>, as indicated in the label.

SiII doublet. As expected, the re-scattered emission component at resonance is reduced significantly compared to the single-scattering approximation resulting in an increased intensity of the fluorescent lines. We note that this effect enhances the contamination of the SiII 1193Å absorption component from re-emitted fluorescent photons from the SiII 1190Å transmission. This enhancement is particularly prevalent in low resolution spectra.

### 2.2. Spherical envelope observed with a circular finite aperture

If the spectroscopic observations are made using an aperture that does not include the full extent of the scattering envelope, then the observed line profile can change dramatically. To illustrate the consequences, we consider here the case of a spherical envelope observed with a circular aperture larger than the central source but smaller than the entire envelope, i.e., with  $R_{\text{aper}} \geq R_{\text{SF}}$  and  $R_{\text{aper}} \leq R_{\text{W}}$ . We also restrict our analysis to  $\gamma = 1$ .

Clearly, the blueshifted absorption component of the

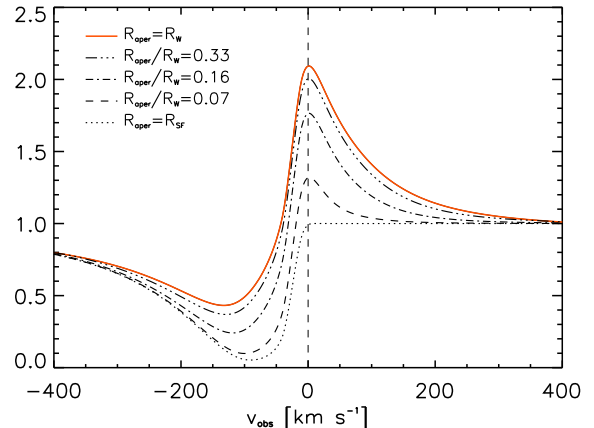


FIG. 6.— The P-Cygni line profile changes as function of size of spectroscopic aperture, from a pure absorption profile ( $R_{\text{aper}} = R_{\text{SF}}$ ), to a classic P-Cyg profile ( $R_{\text{aper}} = R_{\text{W}}$ ). The profiles were computed assuming a spherical expanding envelope,  $\gamma = 1$ ,  $\tau = 60$ ,  $v_0 = 25 \text{ km s}^{-1}$  and  $v_{\infty} = 450 \text{ km s}^{-1}$  (we consider here a line with no fluorescent transition, such as, e.g., SiIII  $\lambda = 1260$ ).

profile will remain unchanged due to the presence of the aperture. The blue and red scattered emission, however, will change. In fact, for a shell of intrinsic velocity  $v$ , the aperture will block those photons scattered at velocities smaller than  $v_{\text{aper}} = v \cos(\theta_{\text{aper}})$ , where  $\theta_{\text{aper}}$  is such that  $\sin(\theta_{\text{aper}}) = R_{\text{aper}}/r_v$ . Clearly, see Figure 1, each shell will correspond to a different  $\theta_{\text{aper}}$ .

In Figure 1 we show the edge-on view of a plane of constant  $v_{\text{obs}}$  (dotted line). As we saw earlier, only layers with  $v \geq v_{\text{obs}}$  will contribute to the emission at  $v_{\text{obs}}$ . Figure 1 shows that the effect of adding a circular aperture is to remove the contribution at  $v_{\text{obs}}$  from all shells with  $v > v_{\text{up}}$ , where:

$$v_{\text{up}} = \frac{v_{\text{obs}}}{\cos\theta_{\text{aper}}}. \quad (23)$$

In terms of  $v_0$ , and after a little algebra, we get:

$$y_{\text{up}}^2 = x^2 + \left(\frac{R_{\text{aper}}}{R_{SF}}\right)^2. \quad (24)$$

Thus,  $I_{em,blue}^{aper}(x)$  (see Eq. 13) can be written here as:

$$I_{em,blue}(x)^{aper} = \int_{\max(x,1)}^{y_{\text{up}}} \frac{1 - e^{-\tau(y)}}{2y} dy; \quad (25)$$

Analogously,  $I_{em,red}^{aper}(x)$  will be:

$$I_{em,red}(x)^{aper} = \int_{y_1}^{y_{\text{up}}} \frac{1 - e^{-\tau(y)}}{2y} dy; \quad (26)$$

In Figure 6 we show how the P-Cygni profile changes with the ratio  $R_{\text{aper}}/R_{SF}$ . In the extreme case of  $R_{\text{aper}}/R_{SF} = 1$  (dotted line), i.e., when the aperture is only as large as the source of continuum, the line is observed only in absorption, and blueshifted relative to the systemic velocity of the galaxy. A component of scattered re-emitted photons coming from the absorbing material is contributing to the blue side of the line, but no re-emitted photons are detected on the red side, because of both the effect of the aperture, and the -often neglected- occultation by the galaxy.

As the ratio  $R_{\text{aper}}/R_{SF}$  increases, fewer photons scattered toward the observer are blocked by the aperture. As a result, the emission component of the profile (centered at the systemic velocity) becomes more and more pronounced. The shape of the absorption profile also changes because of the increasing contribution of photons scattered by material moving toward the observer. It is also evident from Figure 6 that the velocity at maximum absorption shifts toward higher blueshifted velocities as the the contribution from scattered emission increases (i.e., as  $R_{\text{aper}}/R_{SF}$  increases).

### 3. APPLICATION TO REAL SPECTRA

As an example of its flexibility, we apply the SALT model to resonant line profiles observed in a stacked spectrum of Ly $\alpha$  emitting galaxies. We first summarize the data and the measurements (Section 3.1) and then discuss the properties of that outflow that can be inferred from the absorption line analysis performed with the SALT model.

#### 3.1. Data and measurements

The average spectrum modeled in this section was created by stacking Cosmic Origin Spectrograph (COS Green et al. 2012) medium-resolution spectra of a sample of 25 known  $z \sim 0.3$  Ly $\alpha$  emitters (Deharveng et al. 2008; Cowie et al. 2010). The details of the data reduction and spectral extraction are presented in Scarlata et al. (2014). For each galaxy, we have accurate redshift measurements obtained from the H $\alpha$  emission line profiles (Cowie et al. 2011).

To create the stacked spectrum, we first blueshift the observed spectra of individual galaxies into the rest-frame using the measured H $\alpha$  velocities. Then, at each wavelength we compute a flux-weighted average and a standard deviation. The mean stacked UV spectrum (shown after a box-car smoothing of 0.85Å) is shown in Figure 7, where the shaded gray area corresponds to

$\pm$  one weighted standard deviation. In Figure 7, the top panel shows the number of galaxies that entered the stack at each wavelength. In the stacked spectrum we are able to clearly identify and reliably measure the features presented in Tables 2 and 3 and marked in Figure 7. The list includes five absorption lines and four fluorescent emission lines. The list also includes the C III  $\lambda 1175$  absorption line, which is mainly produced in the stellar photospheres.

If we assume that lines are pure absorption and pure emission we could measure the bulk velocity of the gas from the peak velocity of the lines. We derive the peak positions by fitting Gaussian line profiles to the observed absorption/emission lines. When two lines of a given multiplet/ion are blended, we fit them simultaneously constraining the width of the Gaussian function to be the same for both lines. In Figure 8 we zoom-in on the spectral regions around different transitions in the Si<sup>+</sup> and Si<sup>++</sup> ions and plot the resulting best-fit Gaussian models. The errors on the peak wavelength were computed with a Monte Carlo simulation. We created 1000 realizations of the stacked spectrum by changing the flux at each wavelength within  $\pm 1\sigma$ . The new profiles were fitted with a Gaussian, and the error on the peak wavelength was computed as the standard deviation of the 1000 best-fit peak wavelengths.

In Tables 2 and 3 we report the vacuum wavelength of the considered transitions, the observed peak wavelength of the profiles, as well as the velocity shift between the galaxy's rest frame velocity (computed from the H $\alpha$ ) and the peak velocity of the profiles. The stellar C III velocity is consistent with the systemic velocity computed from the H $\alpha$  emission line profiles. Note that the peak/trough velocities obtained from the Gaussian fits offer an easy mathematical representation of the data but do not add immediate physical meaning. The velocity profiles shown in Figure 8 are typical of star forming galaxies at both high and low redshifts (e.g. Shapley et al. 2003; Steidel et al. 2011; Jones et al. 2012; Heckman et al. 2011; Wofford et al. 2013), where they are usually interpreted as originating in a gas outflow probably driven by the current episode of star-formation.

The results of the Gaussian fits presented in Figure 8 would indicate that the gas is moving toward the observers with velocities -as measured at the maximum absorption/emission- ranging between  $-160$  and  $-220\text{km s}^{-1}$ . The average velocity computed in this way from all absorption lines is  $-185 \pm 25\text{ km s}^{-1}$ . The profiles in Figure 8 also show absorption at velocities as high as  $-500\text{km s}^{-1}$ , indicating the presence of multiple velocity components and/or a velocity gradient in the outflowing gas. All detected fluorescent emission lines are blueshifted with respect to the systemic H $\alpha$  velocity with peak velocities ranging between  $-88$  and  $-137\text{km s}^{-1}$ . With an average outflow velocity of  $-100 \pm 22\text{km s}^{-1}$ , the fluorescent emission components appear to have a systematically-lower velocity shift than the resonant absorption lines.

Resonant photons can be either re-emitted at resonance, or in the fluorescent channel, when available. Thus, the two lines originate in the same gas and will share the same kinematical properties. Naively, the measured systematic difference in the bulk velocities of the

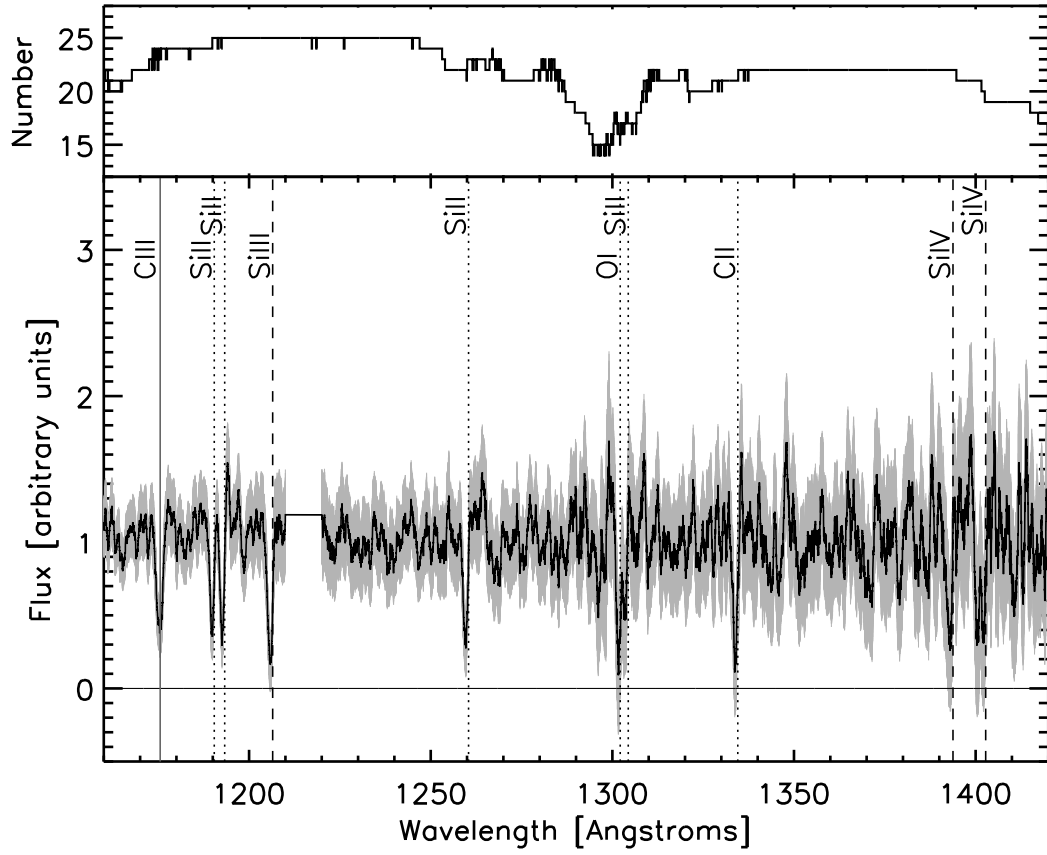


FIG. 7.— Composite rest-frame UV spectrum of 25  $z \sim 0.3$  Ly $\alpha$ -emitting galaxies. Multiple absorption features are identified with vertical lines. Solid lines indicate stellar photospheric absorptions, dotted and dashed lines indicates resonant absorption originating in the galaxy's ISM, with dotted and dashed showing low- and high- ionization metal lines, respectively. The top panel shows the number of galaxies used to compute the average spectrum at each wavelength.

absorption and fluorescent emission lines could then be interpreted as an indication that these lines formed in two kinematically-distinct components. In the following section, we use SALT to consistently model the scattering from the outflowing gas, and show how the systematic velocity difference can be the result of a non-symmetric outflow.

### 3.2. Modeling the line profiles

Here we use SALT to model the observed absorption/emission profiles observed in the stacked spectrum. The free parameters for the models are  $\tau_0$ ,  $v_0$ , and  $v_\infty$  for the spherical outflow, and  $\tau_0$ ,  $v_0$ ,  $v_\infty$  and  $R_{\text{aper}}$ , for the spherical outflow plus aperture. These parameters fully describe the density and velocity field of the galactic outflow, and do not depend on the particular transition within a given ionic species. We therefore constrain the model’s free parameters by simultaneously fitting the four radiative transitions of  $\text{Si}^+$ , observed around  $\lambda = 1190\text{\AA}$ . We chose this spectral region because it shows the highest  $S/N$  of the stacked spectrum, and because of the presence of both two resonant absorption and the corresponding fluorescent emission lines. To model the observed line profiles we use equation 22b, which accounts multiple scattering within each shell as explained in section 2.

We derive the best-fit parameters for the symmetric outflow model with and without a view-limiting aperture, by performing a  $\chi^2$  minimization on the entire doublet profile, including both absorption and emission lines. The models were computed on the same velocity vector as the data, and then box-car smoothed with the same kernel, before proceeding to the computation and minimization of the  $\chi^2$ . The best-fit line profiles for the SiII doublet are shown in Figure 9, and the parameter values are given in Table 4. The blue and red curves show the best fit for the spherical outflow with and without the spectroscopic aperture, respectively.

The simplest spherical models (with or without aperture) well reproduce the depth, shape and central velocities of the blueshifted absorption components of the resonant doublet. This indicates that our simple assumptions for the density and velocity fields of the scattering material are adequate representation of the  $\text{Si}^+$  distribution. On the other hand, the spherical model with no limiting aperture fails to reproduce the observed profiles in two key aspects: 1) it substantially overproduces the amount of scattered emission, and 2), due to the symmetry in the considered configuration, it predicts that the emission component of the P-Cygni profile should be centered at the systemic velocity, while the observations shows that the peaks of the fluorescent emission are clearly blueshifted.

As we discussed in Section 2.2, the effect of a spectroscopic aperture is to selectively decrease the number of scattered photons that are able to reach the observer. As Figure 9 shows (blue curve), adding an aperture alleviates the first of the two discrepancies. However, because of the intrinsic symmetry of the outflow model, the scattered re-emission is still centered at zero velocity, and therefore the model still fails in fully reproducing the observed features. A blueshift in the scattered emission component originating in outflowing material can be obtained if the outflow is not spherically symmetric with

respect to the central source. A simple way to implement this, is by differentially weighting the contribution to the final profile from different portions of the envelope. Thus, we introduce a scaling factor –  $f_{\text{obsc}}$  – to the red component of the scattered profile (Eqn 14); i.e., the radiation scattered in the half sphere moving away from the observer). Physically, the parameter  $f_{\text{obsc}}$  can be used to mimic a face-on galaxy, where the disk is absorbing part of the radiation emitted by the outflowing material (see Section 4). The profile can now be written as:

$$I(x)^{\text{asy}} = 1 - I_{\text{abs}} + I_{\text{emi,blue}} + f_{\text{obsc}} \times I_{\text{emi,red}}. \quad (27)$$

$f_{\text{obsc}}$ , represents the fraction of  $I_{\text{emi,red}}$  that is allowed to reach the observer. We refer to the above profile as the “asymmetric model”, to indicate that the receding half of the expanding envelope is seen less easily than the approaching front part. The best fit asymmetric outflow model is shown in Figure 9 with the yellow line. This model is clearly able to *simultaneously reproduce the relative intensity of the fluorescent emission and resonant absorption lines, as well as their systematically different peak positions.*

We can test our results using a different resonant transition in  $\text{Si}^+$ . The resonant line at  $\lambda = 1260.42$  is ideal for this purpose. As Figure 8 shows, we detect both the resonant absorption and the corresponding fluorescent emission. This absorption originates in the same material where the Si II  $\lambda 1190$  doublet is produced and is thus perfect to test the parameters of the outflow model (i.e., the density, velocity field, and geometry). In Figure 10 we show the observed Si II  $\lambda 1260$  profile, together with the model profile computed using the best-fit outflow parameters derived from our analysis of the 1190–1193 $\text{\AA}$  doublet (i.e., changing only the transition dependent parameters in the profile equations). Figure 10 shows that the model optimized to fit the Si II doublet fully reproduces the observed Si II  $\lambda 1260$  profile as well. In particular, it reproduces both the blueshifted absorption component as well as the intensity and peak wavelength of the fluorescent emission. We stress again that the parameters of the outflow are kept fixed to the best-fit values given in Table 4.

## 4. DISCUSSION

Near and far-UV spectra include numerous resonant metal absorption lines that, combined with the appropriate theoretical tools, provide powerful diagnostics for galactic outflows. High-quality rest-frame UV spectra are currently available for nearby individual galaxies (e.g., with data from the Hubble Space Telescope), and stacked spectra of high-redshift galaxies (with data from 8m class telescopes). Soon, with the planned 30m telescopes, we will be able to study at high resolution absorption line spectra in individual objects up to the highest redshifts.

Resonant blue-shifted UV absorption features are commonly modeled as originating in a thin shell of gas moving at the outflow velocity (as measured from the centroids of resonant absorption lines, e.g., Verhamme et al. 2006; Schaerer & Verhamme 2008; Verhamme et al. 2008; Schaerer et al. 2011). Substantial evidence, however, suggests that this description is

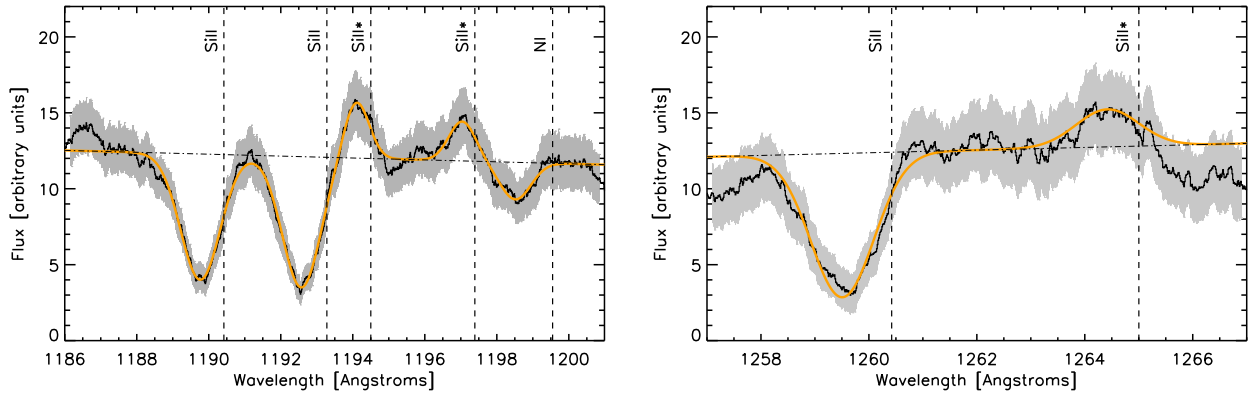


FIG. 8.— Zoom in on the spectral regions around the absorption and emission line features considered in this work. In each panel, the dashed vertical lines show the vacuum wavelength of each transition (as indicated by each label). The orange line shows the sum of the best-fit Gaussian profiles, while the dot-dashed line shows the continuum level.

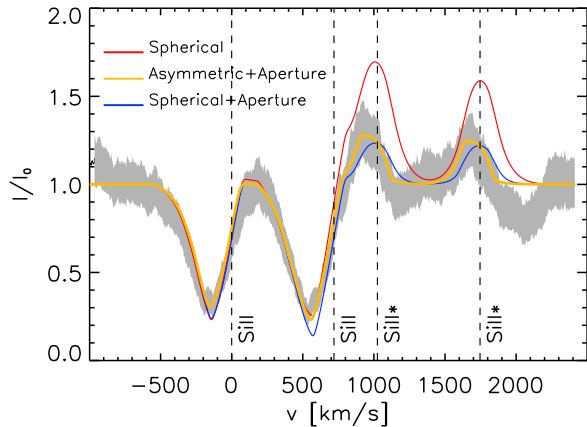


FIG. 9.— The absorption and re-emission profiles of the Si II doublet are well reproduced with an asymmetric model and accounting for the effect of the finite COS aperture size. Best fit model profiles to the Si II 1190–1193Å doublet are shown for different outflow geometries, as indicated in the label. All models shown in this Figure include multiple scattering within each shell.

too simplistic, as noted already by, e.g., Pettini et al. (2002). First of all, when the absorption lines are observed at high enough spectral resolution, they show asymmetric profiles covering a broad range of velocities (up to as much as  $-1000 \text{ km s}^{-1}$ , Tremonti et al. 2007; Diamond-Stanic et al. 2012; Sell et al. 2014). This indicates that the gas is not confined to a thin shell, but rather is distributed in an extended envelope, with velocity and density changing with the distance from the galaxy. More realistic models of extended outflows, with velocity and density gradients have been proposed (e.g., Prochaska et al. 2011; Rubin et al. 2011; Martin et al. 2013), and highlight the importance of properly accounting for the geometry of the outflowing material.

Second, well defined P–Cigny profiles from resonant transitions of MgII, as well as the detection of fluorescent emission associated with resonant transitions of Si II, and FeII, are commonly observed (Shapley et al. 2003; France et al. 2010; Rubin et al. 2011), indicating

that the re-emission component from the outflowing gas cannot be neglected, particularly in compact galaxies or galaxies at high- $z$ , where the spectroscopic aperture may include a substantial fraction of the extended scattering outflow. Neglecting possible contribution from re-emitted photons may have important consequences for the determination of the gas column density and/or covering fraction, as recently noted by, e.g., Prochaska et al. (2011).

The SALT model discussed in this paper provides a simple analytical description of the line profiles originating in the expanding envelopes around galaxies, that properly account for multiple scattering of resonant photons, scattered re-emission, and observational aperture effects.

#### 4.1. On the use of the absorption profiles as indication of covering fraction

In the approximation of pure absorption and with well resolved line profiles, the gas apparent optical depth at a given velocity  $\tau(v)$  is often used to derive the apparent column density profile ( $-\ln(I(v)/I_0(v)) = \tau(v) \propto f\lambda N(v)$ , e.g. Pettini et al. 2002). However, it is well known that the apparent column density obtained from line profiles can be underestimated if undetected saturated components contribute at some velocities. When two or more transitions of a given species differing only in the product of  $f\lambda$  are available, then information about line saturation can be inferred from the comparison of the apparent optical depth profiles (that should be identical within the observational errors). If saturation is present, the line with the highest oscillator strength will result in a lower apparent column density. The previous reasoning is correct only if the absorbing gas fully covers the continuum source. If this is not the case, the line profile will also depend on the gas covering fraction ( $f_C$ ), as well as the optical depth (i.e.,  $I/I_0 = 1 - f_C(1 - e^{-\tau})$ ). Various works have used absorption-line profiles to determine the gas  $f_C$ , under the assumption that absorption lines are saturated (i.e.,  $e^{-\tau} \rightarrow 0$  in  $I/I_0$ , e.g. Jones et al. 2013; Martin & Bouché 2009). When the scattering envelope is included in the spectroscopic aperture, however,

this approach cannot be used: the resonant scattered re-emission affects substantially the residual intensity at line center, in different ways depending on the atomic level structure and the spontaneous transition probabilities.

We show this point in Figure 11, where we present the resonant absorption profiles originating in an outflowing envelope with  $f_c = 1$ , for three transitions of  $\text{Si}^+$ . The top panel shows the absorption component only of the profile: when only absorption is considered, the three profiles scales as expected, according to the value of  $f\lambda$  for each transition. This is not true anymore when the resonant scattered and fluorescent re-emission are included (middle panel): close to the maximum absorption, in fact, the transmission with the lowest value of  $f\lambda$  is in fact the deepest! This is simply due to the relative value of the branching ratios for the resonant and fluorescent channels for these particular transitions. At the largest velocities, where the filling from scattered radiation is less important and the optical depth is smaller, the absorption profiles are again proportional to  $f\lambda$ .

In the bottom panel of Figure 11 we simulate the line profiles as they would be observed with COS, assuming a spectral resolution of  $30\text{ km s}^{-1}$ , and a noise of 10%. Because of the resolution and S/N ratio, the three lines are identical close to the core, and barely distinguishable at the largest velocities. We note, however, that we did not account for uncertainties in the normalization of the spectra, which may affect the profiles, particularly at the largest velocities. The simulated lines also show that from the resonant profiles alone it is hard to identify the presence of scattered re-emission: because at least 50% of the photons are re-emitted in the fluorescent line, for all the transitions considered. However, *the presence of the fluorescent emission is a clear sign-post that the absorption profiles will be affected by emission filling*. Because the strength of the filling depends on the branching ratio for the fluorescent transitions, it is not correct to average together profiles of different lines of the same ion. Moreover, the effect of the filling of the absorption lines will also depend on the *geometry of the outflow* (see Section 3.2) as well as the *relative size of the scattering outflow region and the spectroscopic aperture*.

As an example of what can be achieved by modeling absorption profiles with SALT, we have modeled the UV stacked spectrum of 25  $\text{Ly}\alpha$  emitters in the nearby Universe. The spectrum shows a number of resonant absorption and fluorescent emission lines generating in the  $\text{Si}^+$  in the galaxy’s gaseous medium. The profiles of the resonant absorption lines are systematically blueshifted with respect to the systemic velocity, with an average gas velocity at maximum absorption of  $-185 \pm 25 \text{ km s}^{-1}$ . The peak velocity of the fluorescent emission lines, however, is systematically lower than the outflow velocity obtained from the absorption profiles ( $-100 \pm 22 \text{ km s}^{-1}$ ). We showed with SALT how simple symmetric models fail to reproduce this velocity difference, and asymmetry in the gas distribution needs to be present. Our best fit model with  $f_{\text{obsc}} = 0.1$  describes a geometry in which the half a sphere receding from the observer contributes only 10% to the fluorescent emission, which is then dominated by the emission from the half a sphere

approaching the observer. Physically, this simple model can be used to describe the outflow from a disk galaxy seen approximately face-on, where the radiation scattered from the half-sphere receding from the observer has to go through the opaque disk, that will have an optical depth  $\tau = -\ln(1 - f_{\text{obsc}}) = 2.3$ .

The sample of galaxies that entered the stacked analysis is not randomly selected among starforming objects, but rather it comprises only galaxies showing  $\text{Ly}\alpha$  in emission. The conditions that allow more  $\text{Ly}\alpha$  radiation to escape from a galaxy are still highly debated, with some authors suggesting that age is a dominant factor (e.g., Cowie et al. 2011), while others advocating for dust extinction (e.g. Hayes et al. 2013; Atek et al. 2014). Our result seems to indicate that, on average,  $\text{Ly}\alpha$ -emitters are able to escape more easily in the direction perpendicular to the galaxy disk, than along the disk, suggesting that the viewing angle is also an important factor in determining the  $\text{Ly}\alpha$  escape/visibility. This result is not unexpected, since the direction perpendicular to the galactic disk is also the one that offers the minimum column density of diffuse material, and, thus, of neutral gas (e.g., see Verhamme et al. 2012, for results of radiative transfer simulations of  $\text{Ly}\alpha$  photons in a realistic spiral galaxy). In support of our findings, a recent structural analysis of hundreds of  $\text{Ly}\alpha$  emitters at  $z \sim 2.2$  showed that  $\text{Ly}\alpha$  emitters tend to have smaller ellipticity than galaxies at similar redshift with no  $\text{Ly}\alpha$  emission, reinforcing the idea that  $\text{Ly}\alpha$  photons escape more easily in the direction of minimum optical depth, i.e., minimum hydrogen column density (Shibuya et al. 2014).

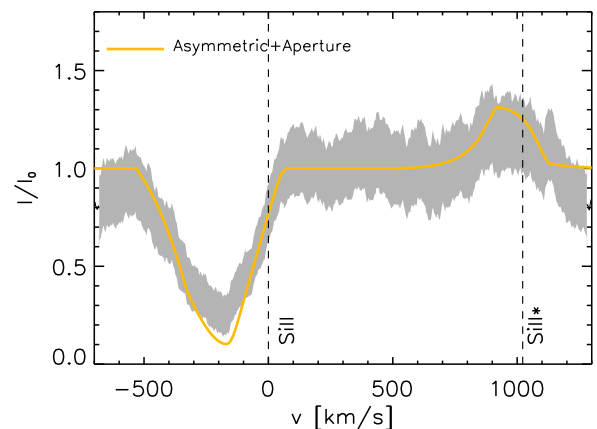


FIG. 10.—  $\text{Si II } \lambda 1260$  absorption line profile and corresponding fluorescent emission, together with the models computed using the best-fit outflow parameters derived from the  $\text{Si II } 1190\text{--}1193\text{ \AA}$  doublet.

## 5. CONCLUSIONS

In this work we have presented and discussed a simple Semi-Analytical Line Transfer model, SALT, to describe the expected absorption and re-emission line profile generated in a spherical outflow surrounding a galaxy with a finite size ( $R_{SF}$ ), under the Sobolev approximation. We derive the analytical profiles computed for the velocity field with the velocity increasing with distance from the galaxy ( $v \propto r^\gamma$ ), and the density radial profile obtained

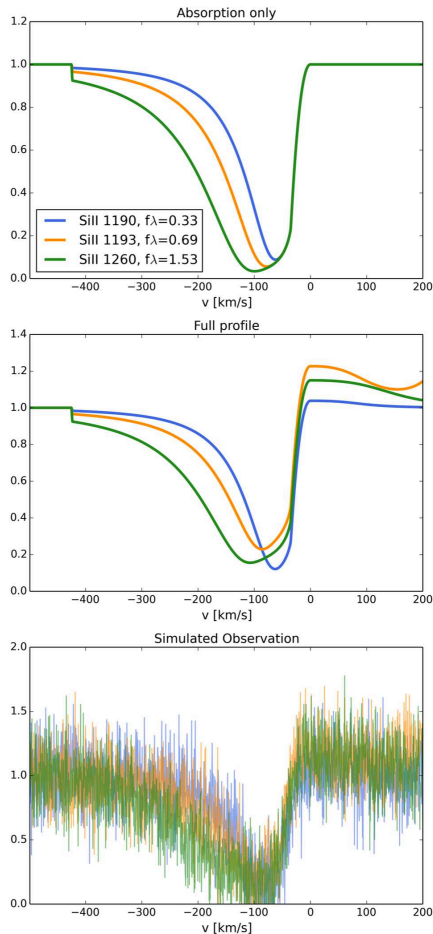


FIG. 11.— Neglecting emission filling of the absorption profiles can cause erroneous conclusions regarding the gas covering fraction. Top: absorption-only components of three resonant transitions of Si+, as indicated in the legend. The model correspond to a spherical envelope with  $v_0 = 35\text{km/s}$ ,  $v_\infty = 450\text{km/s}$ , and  $\tau_{1190\text{\AA}} = 30$ . When only the absorption components are considered, the profiles scale according to the value of  $f\lambda$ . Middle: full line profiles including the scattered re-emission component. Particularly at velocities close to zero, the profiles do not scale as  $f\lambda$  anymore. Bottom: simulated spectrum with 10% errors, and resolution of 30km/s.

assuming a constant mass outflow rate ( $n_i(r) \propto (vr^2)^{-1}$ ). We include the effect of multiple scatterings properly accounting for the atomic structure of the scattering ions. We also discuss how the line profile changes due to the effect of a circular spectroscopic aperture that does not cover the full extent of the outflow (Section 3), and the case in which part of the outflow is obscured.

Our analysis reproduces the main features observed in the profiles generated with more complex radiative transfer codes applied to gaseous outflows with the same geometry (Prochaska et al. 2011). Namely, we show how -for a spherically symmetric outflow- the scattered re-emission is centered at zero velocity and thus alters the shape of the pure absorption component generated in the material in front of the emitting galaxy. Outflow velocities computed from the wavelength of the absorption line

trough do not include this effect. Such an analysis results in an overestimate of the outflow velocity. The intensity of the emission component of the line profile depends not only on the spectroscopic aperture used for the observations, but also on the atomic structure of the particular ion used in the analysis and the spontaneous transition probabilities. In the case of the Si<sup>+</sup> 1190–1193Å doublet, a photon absorbed in the 1190Å transition has a higher chance of being re-emitted in the fluorescent transition to the  $2P^03/2$  level, thus somewhat limiting the “filling” effect on the absorption component.

We have considered the resonance absorption and fluorescent emission profiles observed in the average UV spectrum of 25  $z \sim 0.3$  Ly $\alpha$  emitters. With a simplistic Gaussian profile fit one would find that the average velocities computed from the trough ( $-185 \pm 25 \text{ km s}^{-1}$ ) and the peak wavelengths ( $-100 \pm 22 \text{ km s}^{-1}$ ) of the profiles systematically differ, with the absorption-derived velocity being more negative than the emission-derived velocity. Regardless of the size of the spectroscopic aperture, a symmetric outflow of an arbitrary shape produces a profile with the emission component centered at the systemic velocity of the galaxy, and so cannot explain the systematic difference between the emission and absorption velocities. On the other hand, we used SALT to show that this shifts comes naturally if most of the radiation scattered by the receding half of the outflow is obscured from view. This model can be interpreted as a simple representation of a disk galaxy observed face-on, where the thick disk acts as a semi-transparent screen for the backscattered radiation. This result thus indicates that, on average, galaxies tend to show Ly $\alpha$  in emission more frequently when observed face-on. This idea is supported both by recent observations of high-redshift Ly $\alpha$ -emitting galaxies (Shibuya et al. 2014), as well as high-resolution radiative transfer simulation of Ly $\alpha$  photons in disk galaxies (Verhamme et al. 2012).

To conclude, by simultaneously reproducing both the resonant absorption and the associated resonant and fluorescent emission, the line profiles computed with our SALT model are more far-reaching than a simple absorption-line based analysis. This is especially true when the data show evidence (e.g., the presence of a P-Cygni profile and/or fluorescent emission lines) of scattered re-emission from the galaxy wind. The formalism developed here can be easily extended to other geometries, to account for clumpiness of the outflowing gas (Card et al., in prep), and to different ions/transitions.

We wish to thank our referee for valuable comments that helped us to improve the presentation of our work. CS acknowledges Alaina Henry, Crystal Martin, Dawn Erb, Marc Dijkstra for stimulating discussions. CS acknowledges partial support by HST-GO-12269.01 grant. NP acknowledges partial support by STScI-DDRF grant D0001.82435. CS acknowledges M. Bagley for a careful reading of the manuscript (and pointing out the randomness in the use of commas).

TABLE 1  
ATOMIC DATA FOR Si II AND Si III IONS. DATA TAKEN FROM THE NIST ATOMIC SPECTRA DATABASE<sup>a</sup>.

Ion	Vac. Wavelength Å	$A_{ul}$ $s^{-1}$	$f_{lu}$	$E_l - E_u$ eV	$g_l - g_u$	Lower level Conf., Term, J	Upper level Conf., Term, J
Si II	1190.42	$6.53 \times 10^8$	$2.77 \times 10^{-1}$	0.0 – 10.41520	2 – 4	$3s^2 3p 2P^0 1/2$	$3s 3p^2 2P 3/2$
	1193.28	$2.69 \times 10^9$	$5.75 \times 10^{-1}$	0.0 – 10.39012	2 – 2	$3s^2 3p 2P^0 1/2$	$3s 3p^2 2P 1/2$
	1194.50	$3.45 \times 10^9$	$7.37 \times 10^{-1}$	0.035613 – 10.41520	4 – 4	$3s^2 3p 2P^0 3/2$	$3s 3p^2 2P 3/2$
	1197.39	$1.40 \times 10^9$	$1.50 \times 10^{-1}$	0.035613 – 10.39012	4 – 2	$3s^2 3p 2P^0 3/2$	$3s 3p^2 2P 1/2$
	1260.42	$2.57 \times 10^9$	1.22	0.0 – 9.836720	2 – 4	$3s^2 3p 2P^0 1/2$	$3s^2 3d 2D 3/2$
	1264.73	$3.04 \times 10^9$	1.09	0.035613 – 9.838768	4 – 6	$3s^2 3p 2P^0 3/2$	$3s^2 3d 2D 5/2$

<sup>a</sup><http://www.nist.gov/pml/data/asd.cfm>

<sup>b</sup><http://www.nist.gov/pml/data/asd.cfm>

TABLE 2  
ABSORPTION LINES MEASURED IN THE STACKED SPECTRUM.

Species	Formation	$\lambda_{vac}$ Å	$\lambda_{obs}$ Å	$\Delta v$ <sup>a</sup>
Si II	ISM	1190.42	$1189.83 \pm 0.09$	$-160 \pm 25$
Si II	ISM	1193.29	$1192.60 \pm 0.09$	$-174 \pm 24$
Si II	ISM	1260.42	$1259.56 \pm 0.08$	$-218 \pm 21$
C II	ISM	1334.53	$1333.81 \pm 0.10$	$-164 \pm 24$
Si III	ISM	1206.50	$1205.75 \pm 0.08$	$-188 \pm 20$
C III	Photo	1175.53	$1175.42 \pm 0.1$	$-28 \pm 25$

<sup>a</sup> Velocity shift of the absorption trough with respect to the H $\alpha$  emission line systemic velocity.

TABLE 3  
FLUORESCENT EMISSION LINES MEASURED IN THE STACKED SPECTRUM.

Species	Formation	$\lambda_{vac}$ Å	$\lambda_{obs}$ Å	$\Delta v$ <sup>a</sup>
Si II*	ISM	1194.50	1194.10	-100.2
Si II*	ISM	1197.39	1197.04	-88.2
Si II*	ISM	1265.00	1264.42	-137.5
C II*	ISM	1335.71	1334.53	-55.7

<sup>a</sup> Velocity shift of the absorption trough with respect to the H $\alpha$  emission line systemic velocity.

TABLE 4  
BEST FIT VALUES FOR THE Si II  $\lambda_{1190} - 1193$  DOUBLET.

Model	$v_0$ [km s <sup>-1</sup> ]	$v_\infty$ [km s <sup>-1</sup> ]	$\tau_0$	$\frac{R_{aper}}{R_{SF}}$	$f_{obsc}$
Spherical model full view	38	425	160	...	...
Spherical model – limited view	40	426	120	2	...
Asymmetric model – limited view	55	425	45	3	0.1

#### REFERENCES

- ????  
08. 1  
Atek, H., Kunth, D., Schaerer, D., et al. 2014, A&A, 561, A89  
Castor, J. I. 1970, MNRAS, 149, 111  
Castor, J. I., & Lamers, H. J. G. L. M. 1979, ApJS, 39, 481  
Cowie, L. L., Barger, A. J., & Hu, E. M. 2010, ApJ, 711, 928  
—. 2011, ApJ, 738, 136  
Davé, R., Oppenheimer, B. D., & Finlator, K. 2011, MNRAS, 415, 11  
Deharveng, J.-M., Small, T., Barlow, T. A., et al. 2008, ApJ, 680, 1072  
Diamond-Stanic, A. M., Moustakas, J., Tremonti, C. A., et al. 2012, ApJ, 755, L26  
Erb, D. K., Quider, A. M., Henry, A. L., & Martin, C. L. 2012, ApJ, 759, 26  
France, K., Nell, N., Green, J. C., & Leitherer, C. 2010, ApJ, 722, L80  
Green, J. C., Froning, C. S., Osterman, S., et al. 2012, ApJ, 744, 60  
Grinin, V. P. 2001, Astrophysics, 44, 402  
Hayes, M., Östlin, G., Schaerer, D., et al. 2013, ApJ, 765, L27  
Heckman, T. M., Borthakur, S., Overzier, R., et al. 2011, ApJ, 730, 5  
Jones, T., Stark, D. P., & Ellis, R. S. 2012, ApJ, 751, 51

- Jones, T. A., Ellis, R. S., Schenker, M. A., & Stark, D. P. 2013, *ApJ*, 779, 52
- Kornei, K. A., Shapley, A. E., Martin, C. L., et al. 2013, *ApJ*, 774, 50
- Lilly, S. J., Carollo, C. M., Pipino, A., Renzini, A., & Peng, Y. 2013, *ApJ*, 772, 119
- Martin, C. L. 2005, *ApJ*, 621, 227
- Martin, C. L., & Bouché, N. 2009, *ApJ*, 703, 1394
- Martin, C. L., Shapley, A. E., Coil, A. L., et al. 2012, *ApJ*, 760, 127
- . 2013, *ApJ*, 770, 41
- Mathis, J. S. 1972, *ApJ*, 176, 651
- Oppenheimer, B. D., Davé, R., Kereš, D., et al. 2010, *MNRAS*, 406, 2325
- Pettini, M., Rix, S. A., Steidel, C. C., et al. 2002, *ApJ*, 569, 742
- Prochaska, J. X., Kasen, D., & Rubin, K. 2011, *ApJ*, 734, 24
- Rubin, K. H. R., Prochaska, J. X., Ménard, B., et al. 2011, *ApJ*, 728, 55
- Rubin, K. H. R., Weiner, B. J., Koo, D. C., et al. 2010, *ApJ*, 719, 1503
- Rupke, D. S., Veilleux, S., & Sanders, D. B. 2005, *ApJS*, 160, 115
- Sato, T., Martin, C. L., Noeske, K. G., Koo, D. C., & Lotz, J. M. 2009, *ApJ*, 696, 214
- Savage, B. D., & Sembach, K. R. 1991, *ApJ*, 379, 245
- Schaerer, D., de Barros, S., & Stark, D. P. 2011, *A&A*, 536, A72
- Schaerer, D., & Verhamme, A. 2008, *A&A*, 480, 369
- Scuderi, S., Bonanno, G., di Benedetto, R., Spadaro, D., & Panagia, N. 1992, *ApJ*, 392, 201
- Sell, P. H., Tremonti, C. A., Hickox, R. C., et al. 2014, *MNRAS*, 441, 3417
- Shapley, A. E., Steidel, C. C., Pettini, M., & Adelberger, K. L. 2003, *ApJ*, 588, 65
- Shibuya, T., Ouchi, M., Nakajima, K., et al. 2014, *ArXiv e-prints*, arXiv:1401.1209
- Steidel, C. C., Bogosavljević, M., Shapley, A. E., et al. 2011, *ApJ*, 736, 160
- Steidel, C. C., Giavalisco, M., Pettini, M., Dickinson, M., & Adelberger, K. L. 1996, *ApJ*, 462, L17
- Tremonti, C. A., Moustakas, J., & Diamond-Stanic, A. M. 2007, *ApJ*, 663, L77
- Verhamme, A., Dubois, Y., Blaizot, J., et al. 2012, *A&A*, 546, A111
- Verhamme, A., Schaerer, D., Atek, H., & Tapken, C. 2008, *A&A*, 491, 89
- Verhamme, A., Schaerer, D., & Maselli, A. 2006, *A&A*, 460, 397
- Weiner, B. J., Coil, A. L., Prochaska, J. X., et al. 2009, *ApJ*, 692, 187
- Weinmann, S. M., Pasquali, A., Oppenheimer, B. D., et al. 2012, *MNRAS*, 426, 2797
- Wofford, A., Leitherer, C., & Salzer, J. 2013, *ApJ*, 765, 118